Article

Discovery Medicine 2026; 38(211): 2634–2648
https://doi.org/10.24976/Discov.Med.202638211.207

$CsSn_{0.5}Pb_{0.5}Br_3$@CS-FA Nanoparticles as a Fluorescent Tracer for the Preliminary Diagnosis of Leptomeningeal Carcinomatosis

Jian Li[1,2,3,4], Yu Zhang[1,2,3], Rongrong Yan[5], Siyu Chen[1,2,3], Ruohao Li[1,2,3], Yinan Jiao[5], Hui Bu[1,2,3,*]

[1]Department of Neurology, The Second Hospital of Hebei Medical University, 050000 Shijiazhuang, Hebei, China
[2]Key Laboratory of Clinical Neurology (Hebei Medical University), Ministry of Education, 050000 Shijiazhuang, Hebei, China
[3]Neurological Laboratory of Hebei Province, 050000 Shijiazhuang, Hebei, China
[4]General Practice Department, Hengshui People's Hospital, 053000 Hengshui, Hebei, China
[5]Institute of Materials for Energy Conversion, School of Materials Science and Engineering, Shijiazhuang Tiedao University, 050043 Shijiazhuang, Hebei, China
*Correspondence: 26500825@hebmu.edu.cn (Hui Bu)
Submitted: 2 June 2026 Revised: 3 July 2026 Accepted: 20 July 2026 Published: 24 August 2026

Background: Leptomeningeal carcinomatosis (LC) remains difficult to diagnose at an early stage because current diagnostic approaches rely primarily on magnetic resonance imaging and cerebrospinal fluid (CSF) cytology, which may lack sensitivity or require repeated testing. This study aimed to develop a water-stable, biocompatible, and tumor-targeted fluorescent nanoparticle for the preliminary diagnosis of LC.

Methods: $CsSn_{0.5}Pb_{0.5}Br_3$@CS-FA nanoparticles were synthesized using a water-triggered strategy and characterized by X-ray diffraction, Fourier-transform infrared spectroscopy, transmission electron microscopy, photoluminescence spectroscopy, ultraviolet-visible spectroscopy, and *in vivo* imaging. Their water stability, *in vitro* targeting ability, cytocompatibility, *in vivo* tumor-targeting capacity, and biosafety were evaluated using Lewis lung carcinoma (LLC) cells, C2C12 cells, C57BL/6JNifdc mouse models, and clinical CSF samples. CSF samples from 7 patients with LC and 7 non-LC controls were incubated with the nanoparticles, and fluorescence intensity was detected by flow cytometry.

Results: $CsSn_{0.5}Pb_{0.5}Br_3$@CS-FA nanoparticles showed a stable core-shell structure and maintained fluorescence in aqueous solution for up to 329 days. *In vitro* imaging demonstrated stronger fluorescence in LLC cells than in C2C12 cells, and $CsSn_{0.5}Pb_{0.5}Br_3$@CS-FA produced significantly higher fluorescence than non-targeted $CsSn_{0.5}Pb_{0.5}Br_3$@CS nanoparticles ($p < 0.001$). Cell viability remained above 90% after treatment with 200 μg/mL $CsSn_{0.5}Pb_{0.5}Br_3$@CS-FA. In tumor-bearing mice, fluorescence signals were detectable after injection, peaked at 24 h, and were no longer detectable at 216 h. Hematological, hepatic, renal, histological, and body-weight assessments showed no obvious biosafety concerns. In clinical CSF samples, the fluorescence intensity was markedly higher in the LC group than in the non-LC group (47.08% ± 13.56% vs. 2.75% ± 1.12%, $p < 0.001$).

Conclusion: $CsSn_{0.5}Pb_{0.5}Br_3$@CS-FA nanoparticles exhibited favorable water stability, tumor-targeting ability, fluorescence performance, and preliminary biosafety. Their enhanced fluorescence signal in LC-derived CSF samples suggests potential value as an auxiliary fluorescent tracer for LC diagnosis, although further validation in larger clinical studies is required.

Keywords: leptomeningeal carcinomatosis; perovskite nanoparticles; fluorescent tracer; folic acid; chitosan; cerebrospinal fluid

Introduction

Cancer remains a major barrier to extending life expectancy worldwide, with increasing incidence and mortality [1,2]. Early diagnosis is essential for improving curative opportunities and survival, particularly for aggressive tumors and malignancies with subtle or absent early symptoms [1,2]. Leptomeningeal carcinomatosis (LC) is a severe metastatic complication involving tumor dissemination to the leptomeninges and cerebrospinal fluid (CSF). At present, the diagnosis of LC usually depends on a combination of clinical manifestations, magnetic resonance imaging (MRI), and CSF examination. These procedures can be time-consuming, costly, and insufficiently sensitive to early or subtle disease, which may lead to delayed diagnosis or misdiagnosis [3]. Therefore, more specific and practical strategies are needed for LC diagnosis.

Recent advances in nanomaterials have created opportunities for developing novel diagnostic and therapeutic tools in oncology [4]. Nanoparticle-based optical imaging has developed rapidly as a non-invasive strategy for tumor detection [5,6]. Near-infrared fluorescent probes can

provide deeper tissue penetration and better spatial resolution than visible or ultraviolet probes [7]. However, clinical translation remains limited by toxicity, low quantum yield, and high cost [8]. Inorganic halide perovskite nanocrystals, represented by CsPbX3, have attracted considerable attention for their high photoluminescence quantum yield, narrow emission bandwidth, and tunable band gap [9,10]. They have been explored in optoelectronics, neuromorphic devices, and biomedical imaging [11]. Nevertheless, their applications in bioimaging are hindered by three major challenges: poor stability in aqueous biological environments, the potential cytotoxicity associated with Pb ions, and insufficient tumor-cell targeting.

To address these issues, the present study designed $CsSn_{0.5}Pb_{0.5}Br_3$@CS-FA nanoparticles for LC-related fluorescence detection. Chitosan (CS), a biocompatible and degradable polysaccharide, was used as a protective coating to improve water stability [12]. Partial substitution of Pb by Sn was used to reduce potential Pb-associated toxicity [13]. Folic acid (FA) was conjugated to the nanoparticle surface because FA has high affinity for folate receptors, which are overexpressed in many tumor cells but are limited in most non-cancerous cells [14,15]. Because approximately 9–25% of patients with lung cancer may develop LC, Lewis lung carcinoma (LLC) cells were used in the experimental system. We synthesized $CsSn_{0.5}Pb_{0.5}Br_3$@CS-FA nanoparticles and assessed their structural characteristics, water stability, tumor targeting, biosafety, and preliminary diagnostic performance in clinical CSF samples.

Methods

Materials, Cells, and Animals

LLC cells and mouse myoblast C2C12 cells were purchased from Nanjing Cobioer Biosciences Co., Ltd. (Nanjing, China) (Cat. No. 1101MOU-PUMC000673, Batch No. 1101MOU-PUMC000099). Both cell lines were cultured in high-glucose Dulbecco's modified Eagle's medium (DMEM; Beijing Solarbio Science & Technology Co., Ltd., Beijing, China) supplemented with 10% fetal bovine serum (FBS; ExCell Bio, Taicang, China, Cat. No. FSP500, Lot No. 20240301) and 1% penicillin-streptomycin solution (Beijing Solarbio Science & Technology Co., Ltd., Beijing, China, Cat. No. P1400, Lot No. 20240516). Cells were maintained in a humidified incubator at 37 °C with 5% CO_2. To prevent cell contamination and ensure the stability of cell lines, routine mycoplasma testing was performed using a polymerase chain reaction (PCR)-based mycoplasma detection kit (Yeasen Biotechnology, Shanghai, China) (Cat. No. 40601ES20) at monthly intervals, and all results were negative throughout the study. Cell line identity was confirmed using short tandem repeat (STR) profiling by the supplier, and the profiles were consistent with the reference databases for LLC and C2C12 cells.

Male C57BL/6JNifdc mice aged 6–8 weeks were obtained from Beijing Vital River Laboratory Animal Technology Co., Ltd. (Beijing, China). All mice were housed under specific environmental conditions, with a room temperature of 22 ± 1 °C and relative humidity of 40%–70% (12-h light/12-h dark cycle). Animal experiments were approved by the Ethics Committee of the Second Hospital of Hebei Medical University (No. 2023-AE085) and conducted in accordance with the National Institutes of Health Guide for the Care and Use of Laboratory Animals. All procedures were performed with efforts to minimize animal suffering. At the end of the experiment, mice were euthanized by cervical dislocation under deep anesthesia induced by intraperitoneal injection of 1.25% tribromoethanol (Avertin®) at a dose of 0.2 mL per 10 g body weight. Anesthesia depth was confirmed by the absence of the toe-pinch reflex, and death was confirmed by the absence of spontaneous breathing, heartbeat, and pain reflexes before tissue collection.

Cesium carbonate (Cs_2CO_3, 99%) (Cat. No. C105061; CAS: 534-17-8; Lot No. A2403011), lead bromide ($PbBr_2$, 99%) (Cat. No. L407121; CAS: 10031-22-8; Lot No. L2404152), 1-octadecene (ODE, >90%) (Cat. No. O109487; CAS: 112-88-9; Lot No. O2402283), cyclohexane (C_6H_{12}, 99.5%) (Cat. No. C1521198; CAS: 110-82-7; Lot No. C2405071), oleic acid (OA, ≥99%) (Cat. No. O108485; CAS: 112-80-1; Lot No. O2403222), oleylamine (OAm, 80%–90%) (Cat. No. O106967; CAS: 112-90-3; Lot No. O2401194), folic acid (FA, >97%) (Cat. No. F103639; CAS: 59-30-3; Lot No. F2404091), 1-(3-dimethylaminopropyl)-3-ethylcarbodiimide hydrochloride (EDC) (Cat. No. E106172; CAS: 25952-53-8; Lot No. E2405132), N-hydroxysuccinimide (NHS) (Cat. No. H109330; CAS: 6066-82-6; Lot No. H2402073), dimethyl sulfoxide (DMSO) (Cat. No. D755902; CAS: 67-68-5; Lot No. D2403181), glacial acetic acid (≥99.8%) (Cat. No. A116167; CAS: 64-19-7; Lot No. A2404262), xylene (99%) (Cat. No. X112051; CAS: 1330-20-7; Lot No. X2405031), neutral balsam (Cat. No. N116470; CAS: 96949-21-2; Lot No. N2401303), and ethanol (99.5%) (Cat. No. E111963; CAS: 64-17-5; Lot No. E2402211) were purchased from Aladdin Reagent Co., Ltd. (Shanghai, China). Tin (II) bromide ($SnBr_2$, 99.99%) (Cat. No. T913631; CAS: 10031-24-0; Lot No. M2403072), methyl acetate (98%) (Cat. No. M821446; CAS: 79-20-9; Lot No. M2404129), and ethyl acetate (99%) (Cat. No. E809174; CAS: 141-78-6; Lot No. M2405094) were purchased from Shanghai Macklin Biochemical Co., Ltd. (Shanghai, China). Chitosan (molecular weight, 100,000–300,000) (Cat. No. 594839; CAS: 9012-76-4; Lot No. 995947) was obtained from J&K Scientific Ltd. (Beijing, China). Phosphate-buffered saline (PBS) (Cat. No. P1000; Lot No. 1022Q021), trypsin (Cat. No. T1300; Lot No. 3174657), and high-glucose DMEM (Cat. No. 11965; Lot No. 1967577) were obtained from Beijing So-

larbio Science & Technology Co., Ltd. The Cell Counting Kit-8 (CCK-8) assay kit (Cat. No. C0038; Lot No. CK240615) and Lyso-Tracker Red (Cat. No. C1046; Lot No. LT240528) were purchased from Beyotime Biotechnology Co., Ltd. (Shanghai, China). The Calcein-AM/PI live/dead cell staining kit (Cat. No. 40747ES76; Lot No. 20240315) was purchased from Yeasen Biotechnology Co., Ltd. (Shanghai, China). The 4% paraformaldehyde solution (Cat. No. C516337; CAS: 30525-89-4; Lot No. B5404120) was obtained from Sangon Biotech Co., Ltd. (Shanghai, China). Antifade mounting medium containing 4′,6-diamidino-2-phenylindole (DAPI) (Cat. No. S2110; Lot No. 20240618S) was purchased from Beijing Solarbio Science & Technology Co., Ltd. 1.25% tribromoethanol (Cat. No. M2910; Lot No. NJ24M291007) was purchased from Nanjing Aibei Biotechnology Co., Ltd. Hematoxylin and eosin staining reagents (Cat. No. C0105S; Lot No. 112818190403) were purchased from Beyotime Biotechnology Co., Ltd. The BD Cytofix/Cytoperm™ Fixation/Permeabilization Kit was obtained from BD Biosciences (Franklin Lakes, NJ, USA) (Cat. No. 554714; Lot No. 7346888).

The main instruments used in this study included a Lab2000 glove box system (Etelux Inert Gas System Co., Ltd., Beijing, China) (Model No. Lab2000/2400/750), an FA2104N electronic analytical balance (Shanghai Jingke Tianmei Scientific Instrument Co., Ltd., Shanghai, China), a C-MAG HS 7 magnetic stirrer (IKA, Staufen, Germany), a KQ-100DE ultrasonic cleaner (Kunshan Ultrasonic Instruments Co., Ltd., Kunshan, China), and a TG16G high-speed benchtop centrifuge (Jintan Gaoke Instrument Factory, Changzhou, China). Cell and tissue imaging was performed using an IX71 inverted fluorescence microscope (Olympus, Tokyo, Japan), an FV1000 confocal microscope (Olympus, Tokyo, Japan), and an *In Vivo* Imaging System (IVIS) Lumina III *in vivo* imaging system (PerkinElmer, Waltham, MA, USA). Flow cytometry was conducted using an Attune NxT flow cytometer (Thermo Fisher Scientific, Waltham, MA, USA). Hematological and biochemical analyses were performed using a URIT-5160Vet automated hematology analyzer (URIT Medical Electronic Co., Ltd., Guilin, China), a Celercare M5 automatic biochemical analyzer (MNCHIP Technologies Co., Ltd., Tianjin, China), and a VERSAmax microplate reader (Molecular Devices, San Jose, CA, USA). Nanoparticle characterization was performed using an FEI Talos F200S transmission electron microscope (Thermo Fisher Scientific, Waltham, MA, USA), a D8 ADVANCE X-ray diffractometer (Bruker, Karlsruhe, Germany), a UV/Vis 1050 spectrophotometer (Lambda, USA), a DZF vacuum drying oven (Beijing Kewei Yongxing Instrument Co., Ltd., Beijing, China), and an FS5 fluorescence spectrometer (Edinburgh Instruments, Livingston, UK).

Synthesis of $CsSn_{0.5}Pb_{0.5}Br_3$, $CsSn_{0.5}Pb_{0.5}Br_3$@CS, and $CsSn_{0.5}Pb_{0.5}Br_3$@CS-FA nanoparticles

For the synthesis of $CsSn_{0.5}Pb_{0.5}Br_3$ nanocrystals (NCs), 0.5 mmol $PbBr_2$ and 0.5 mmol $SnBr_2$ were dissolved in 0.5 mL 1-octadecene, followed by the addition of 1 mL oleic acid and 1.5 mL oleylamine. The mixture was stirred at 120 °C until complete dissolution to obtain a precursor solution. Separately, 0.16 g Cs_2CO_3 was added to 1 mL oleic acid and 16 mL 1-octadecene and stirred at 120 °C until full dissolution to prepare cesium oleate. The cesium oleate solution was injected into the precursor solution. After the reaction became turbid white, the mixture was cooled in a water bath to room temperature and centrifuged at 6000 rpm for 15 min. The precipitate was collected, dispersed in 20 mL cyclohexane, and sonicated for 30 min to obtain zero-dimensional $Cs_4Pb_{0.5}Sn_{0.5}Br_6$ NCs, which were stored at 4 °C. The solution was diluted with cyclohexane, mixed with deionized water under vigorous stirring, and sonicated for 1–5 min until the color stabilized. After filtration through a 0.22-micrometer (μm) membrane filter, the filtrate was collected as the $CsSn_{0.5}Pb_{0.5}Br_3$ NC solution.

For preparation of $CsSn_{0.5}Pb_{0.5}Br_3$@CS nanoparticles, 0.1 g chitosan was dissolved in 99 mL deionized water containing 1 mL glacial acetic acid to obtain a 0.001 g/mL CS solution. One milliliter of CS solution was slowly added dropwise to 5 mL $Cs_4Pb_{0.5}Sn_{0.5}Br_6$ NC solution under vigorous stirring. After the solution color changed from white to green and stabilized, the mixture was sonicated for 1–5 min and filtered through a 0.22-μm membrane filter. The filtrate was precipitated with methyl acetate at a volume ratio of 1:2, and the precipitate was dried under vacuum at 40 °C for 6 h to obtain $CsSn_{0.5}Pb_{0.5}Br_3$@CS powder.

For the synthesis of $CsSn_{0.5}Pb_{0.5}Br_3$@CS-FA nanoparticles, 0.005 g FA was dissolved in 5 mL dimethyl sulfoxide. EDC (0.066 g) and NHS (0.036 g) were then added, and the mixture was stirred at room temperature for 2 h to obtain an activated FA solution. The FA solution was mixed with the CS solution and reacted at room temperature for 16 h to obtain the CS-FA solution. One milliliter of CS-FA solution was added to 5 mL $Cs_4Pb_{0.5}Sn_{0.5}Br_6$ NC solution. After the color changed from white to green and stabilized, the mixture was sonicated for 1–5 min and filtered through a 0.22-μm membrane filter. The filtrate was precipitated with ethyl acetate at a volume ratio of 1:2 and vacuum-dried at 40 °C for 6 h to obtain $CsSn_{0.5}Pb_{0.5}Br_3$@CS-FA powder.

Characterization of Nanoparticles

Transmission electron microscopy (TEM; FEI Talos F200S) was used to observe the morphology of $CsSn_{0.5}Pb_{0.5}Br_3$ and $CsSn_{0.5}Pb_{0.5}Br_3$@CS-FA nanoparticles. Fourier-transform infrared spectroscopy (FTIR) spectra were recorded using a Fourier-transform infrared spectrometer to analyze CS, FA, $CsSn_{0.5}Pb_{0.5}Br_3$, and

$CsSn_{0.5}Pb_{0.5}Br_3$@CS-FA nanoparticles. X-ray diffraction (XRD; D8 ADVANCE) was used to characterize the crystal structure of $CsSn_{0.5}Pb_{0.5}Br_3$ and $CsSn_{0.5}Pb_{0.5}Br_3$@CS-FA nanoparticles.

Water Stability Assay

Ultraviolet-visible absorption spectra and photoluminescence (PL) spectra of $CsSn_{0.5}Pb_{0.5}Br_3$@CS-FA nanoparticles were measured using a UV/Vis 1050 spectrophotometer (PerkinElmer, Waltham, MA, USA) and an FS5 fluorescence spectrometer (Edinburgh Instruments, Livingston, UK), respectively. An IVIS Lumina III imaging system was used to monitor changes in fluorescence intensity of $CsSn_{0.5}Pb_{0.5}Br_3$@CS-FA nanoparticles in water from day 0 to day 329.

In Vitro Targeting and Biocompatibility Assays

For confocal imaging, cell slides were placed in 24-well plates and LLC cells or C2C12 cells were seeded at approximately 2×10^4 cells per well. After incubation for 24 h, the medium was replaced with medium containing $CsSn_{0.5}Pb_{0.5}Br_3$@CS or $CsSn_{0.5}Pb_{0.5}Br_3$@CS-FA nanoparticles at 200 μg/mL. After 6 h of incubation, cells were washed three times with PBS, stained with Lyso-Tracker Red (75 nM) at 37 °C for 45 min, washed again, fixed with 4% paraformaldehyde for 30 min, and mounted with antifade mounting medium containing DAPI. Confocal microscopy was performed using 405 nm excitation for DAPI, 488 nm excitation for nanoparticle green fluorescence, and 559 nm excitation for Lyso-Tracker Red. Images were acquired using fixed laser power and detector gain settings across all samples to ensure comparability.

For Calcein-AM/PI staining, LLC cells were seeded in 6-well plates and cultured to approximately 50–60% confluence. Cells were treated with 0 or 200 μg/mL $CsSn_{0.5}Pb_{0.5}Br_3$@CS-FA nanoparticles for 24 h. After collection and washing, cells were resuspended at 1×10^5 to 1×10^6 cells/mL. Two hundred μL of staining solution was mixed with 400 μL of the cell suspension and incubated at 37 °C for 10 min. Fluorescence microscopy was used to detect green fluorescence from viable cells (excitation 488 nm, emission 515 ± 15 nm) and red fluorescence from dead cells.

For the CCK-8 assay, LLC cells were seeded into 96-well plates at 1×10^4 cells per well and cultured for 24 h (n = 6 wells per concentration). Cells were then treated with $CsSn_{0.5}Pb_{0.5}Br_3$@CS-FA nanoparticles at 0, 100, 150, 200, 250, 300, 400, or 500 μg/mL for 24 h. After washing with PBS, 10 μL of CCK-8 solution was added to each well, and cells were incubated for 2 h. Absorbance was measured at 450 nm using a VERSAmax microplate reader (Molecular Devices, San Jose, CA, USA). Cell viability was calculated as $[(As - Ab)/(Ac - Ab)] \times 100\%$, where As is the absorbance of the experimental well, Ab is the absorbance of the blank well, and Ac is the absorbance of the control well.

In Vivo Targeting and Biosafety Evaluation

To establish the subcutaneous tumor model, each C57BL/6JNifdc mouse was injected subcutaneously with 1×10^6 LLC cells into the right anterior chest wall. When the tumor volume reached approximately 100 mm^3, mice received a tail-vein injection of $CsSn_{0.5}Pb_{0.5}Br_3$@CS-FA nanoparticles (200 μL, 4 mg/mL), and fluorescence imaging was performed using IVIS Lumina III before and after injection.

For biosafety evaluation, 10 healthy C57BL/6JNifdc mice were randomly assigned to the control group or the $CsSn_{0.5}Pb_{0.5}Br_3$@CS-FA group (n = 5 per group). Mice were allocated to groups using a computer-generated random number sequence. The investigator performing the *in vivo* imaging and outcome assessments was blinded to group assignment. Mice received three tail-vein injections at 5-day intervals. Body weight was monitored every 4 days. After 1 month, blood samples from three mice in each group were randomly collected for routine blood testing and liver and renal function analysis. The remaining two mice in each group were euthanized by cervical dislocation under deep anesthesia, and death was confirmed before collection of the heart, liver, spleen, lung, and kidney for hematoxylin-eosin (H&E) staining. Fresh tissues were fixed in 4% paraformaldehyde, dehydrated through graded ethanol, cleared in xylene, embedded in paraffin, sectioned, stained with hematoxylin and eosin, dehydrated, cleared, mounted, and observed under a light microscope.

Clinical CSF Samples and Fluorescence Detection

Clinical samples were obtained from 14 patients hospitalized in the Department of Neurology, the Second Hospital of Hebei Medical University, between January 2023 and November 2023, including 7 patients with LC and 7 non-LC controls. The clinical study was approved by the Ethics Committee of the Second Hospital of Hebei Medical University (No. 2023-R360). Written informed consent was obtained from all patients or their legal representatives. The study was conducted in accordance with the Declaration of Helsinki, and all samples were anonymized before testing and analysis.

LC was diagnosed according to the 2023 guidelines issued by the European Association of Neuro-Oncology-European Society for Medical Oncology (EANO-ESMO) [16]. The inclusion criteria for LC were as follows: (1) clinical manifestations involving the brain or spinal cord; (2) a definite tumor history or discovery of tumor after neurological manifestations; (3) typical MRI features showing linear meningeal enhancement with or without nodular enhancement; and (4) positive CSF cytology or positive meningeal biopsy. Patients meeting criteria 1–4 or criterion 4 alone were diagnosed as confirmed LC, whereas patients meeting criteria 1–3 were diagnosed as probable LC. Patients not meeting the diagnostic criteria were included in the non-LC group.

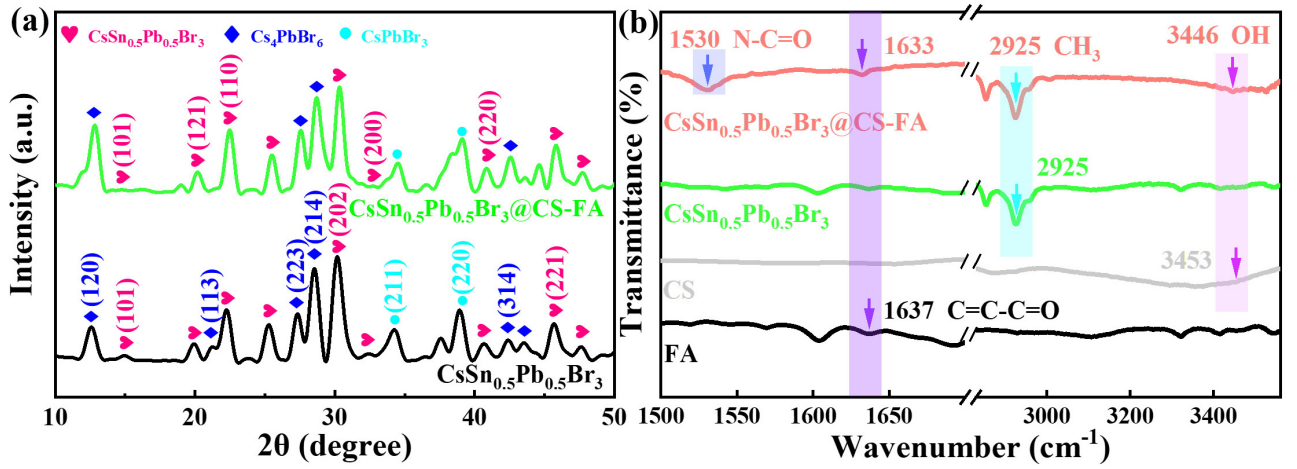

Fig. 1. Structural characterization of the nanoparticles. (a) XRD spectra of $CsSn_{0.5}Pb_{0.5}Br_3$@CS-FA and $CsSn_{0.5}Pb_{0.5}Br_3$. (b) FTIR spectra of $CsSn_{0.5}Pb_{0.5}Br_3$@CS-FA and $CsSn_{0.5}Pb_{0.5}Br_3$. All figures in this manuscript were generated using Origin 2018 (OriginLab Corporation, Northampton, MA, USA). XRD, X-ray diffraction; FTIR, Fourier-transform infrared spectroscopy.

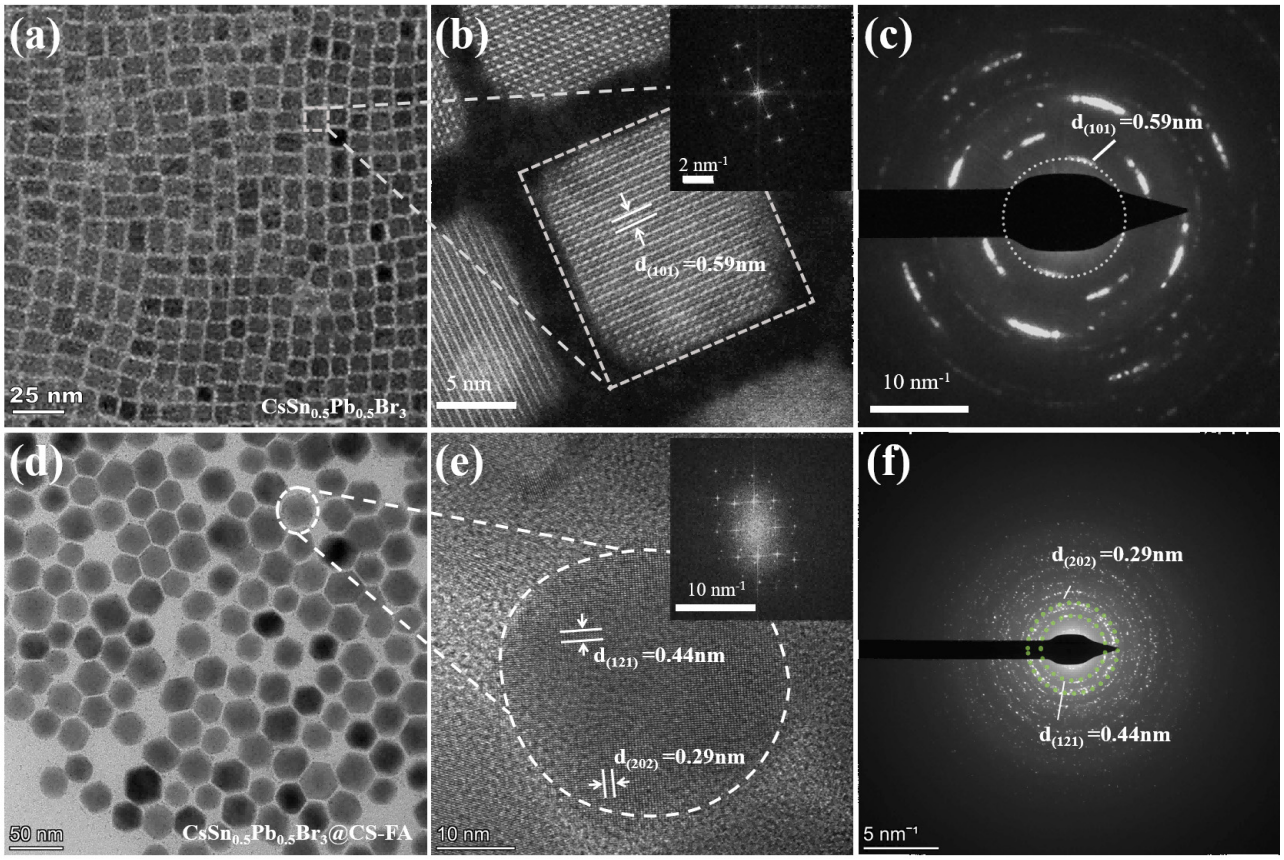

Fig. 2. TEM images of $CsSn_{0.5}Pb_{0.5}Br_3$ and $CsSn_{0.5}Pb_{0.5}Br_3$@CS-FA nanoparticles. (a) TEM, (b) HRTEM, and fast Fourier transform image of $CsSn_{0.5}Pb_{0.5}Br_3$. (c) Selected-area electron diffraction image of $CsSn_{0.5}Pb_{0.5}Br_3$. The scale bar unit (10 nm^{-1}) corresponds to reciprocal space; the measured radius of the diffraction ring yields a real-space interplanar spacing of d = 1/R ≈ 0.59 nm, consistent with the (101) plane identified by XRD. (d) TEM, (e) HRTEM, and fast Fourier transform image of $CsSn_{0.5}Pb_{0.5}Br_3$@CS-FA. (f) Selected-area electron diffraction image of $CsSn_{0.5}Pb_{0.5}Br_3$@CS-FA. TEM, Transmission electron microscopy; HRTEM, high-resolution transmission electron microscopy.

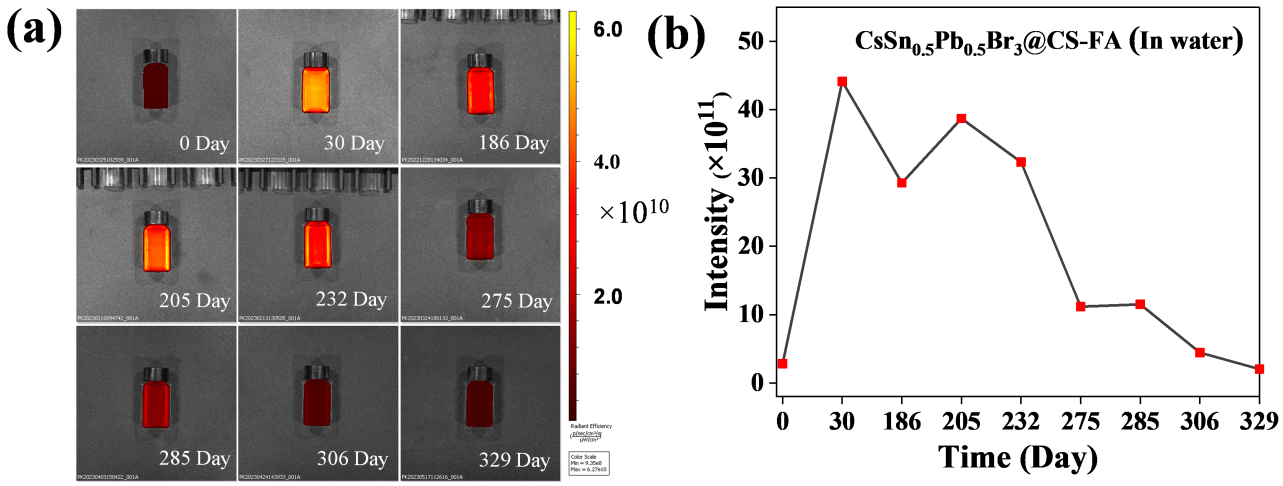

Fig. 3. Long-term fluorescence stability of $CsSn_{0.5}Pb_{0.5}Br_3$@CS-FA nanoparticles in water. (a) IVIS images of $CsSn_{0.5}Pb_{0.5}Br_3$@CS-FA nanoparticle powder dispersed in deionized water. (b) Quantification of fluorescence signal intensity from IVIS images.

For fluorescence detection, 8 mL fresh CSF from each patient was centrifuged at 600 ×g for 5 min, and the precipitate was collected. Each flow tube received 25 µL of $CsSn_{0.5}Pb_{0.5}Br_3$@CS-FA nanoparticles (4 mg/mL), resulting in a final concentration of 200 µg/mL. Samples were incubated at room temperature for 4 h, washed with 2 mL PBS, and centrifuged at 600 ×g for 5 min. Washing and centrifugation were repeated three times. The precipitated cells were resuspended and analyzed by flow cytometry to determine nanoparticle fluorescence intensity. Flow cytometric analysis was performed using an Attune NxT flow cytometer equipped with a 488 nm solid-state laser. For each sample, 10,000 events were collected. The positive threshold was defined based on untreated CSF cells (without nanoparticle incubation) as the negative control group; events with fluorescence intensity above the 99th percentile of the negative control were classified as positive. Non-targeted $CsSn_{0.5}Pb_{0.5}Br_3$@CS nanoparticle-treated samples were used as an additional control to assess non-specific binding. The fluorescence percentage reported herein represents the proportion of positive cells (i.e., the ratio of events exceeding the predefined fluorescence threshold to the total number of events collected, expressed as a percentage). Single-color unstained controls were used for compensation calibration. Flow data were analyzed using Attune Cytometric Software (Thermo Fisher Scientific).

Statistical Analysis

Each experiment was repeated at least three times independently (n = 3 independent biological replicates per experimental group unless otherwise specified). Data are presented as mean ± standard deviation (SD). Normality of data distribution was assessed using the Shapiro–Wilk test, and homogeneity of variances was evaluated using Levene's test; all datasets met the assumptions for parametric testing. Statistical analyses were performed using Origin 2018 (OriginLab Corporation, Northampton, MA, USA) and GraphPad Prism 8.0 (GraphPad Software, San Diego, CA, USA). Comparisons between two groups were performed using Student's *t*-test, and comparisons among multiple groups were performed using two-way analysis of variance (ANOVA) followed by Tukey's post hoc test for multiple comparisons. All statistical tests were two-sided unless otherwise specified. ImageJ software (version 1.54f, National Institutes of Health, Bethesda, MD, USA) was used for quantitative fluorescence intensity analysis. A value of $p < 0.05$ was considered statistically significant.

Results

Synthesis and Characterization of $CsSn_{0.5}Pb_{0.5}Br_3$@CS-FA Nanoparticles

The crystal structure of $CsSn_{0.5}Pb_{0.5}Br_3$@CS-FA and $CsSn_{0.5}Pb_{0.5}Br_3$ was characterized by XRD (Fig. 1a). Peaks at 12.8°, 21.2°, 27.3°, 28.6°, and 42.6° corresponded to the (120), (113), (223), (214), and (314) planes of Cs4PbBr6, respectively [17]. Peaks corresponding to the (211) and (220) planes of CsPbBr3 were also observed at 34.2° and 38.9° [17]. Because the ionic radius of Sn^{2+} is slightly smaller than that of Pb^{2+}, peaks at 14.7°, 20.2°, and 30.3° were assigned to the (101), (121), and (202) planes of $CsSn_{0.5}Pb_{0.5}Br_3$ [18,19,20,21,22,23,24,25,26]. Additional peaks at 22.4°, 32.7°, 40.8°, and 45.8° corresponded to the (110), (200), (220), and (221) planes [17], highlighting successful preparation of $CsSn_{0.5}Pb_{0.5}Br_3$ NCs [19]. Residual zero-dimensional Cs4PbBr6 NCs dispersed in cyclohexane were partially transformed into three-dimensional CsPbBr3 NCs because Sn^{2+} could not completely replace Pb^{2+} [27,28,29]. The broader context of lead-free perovskite

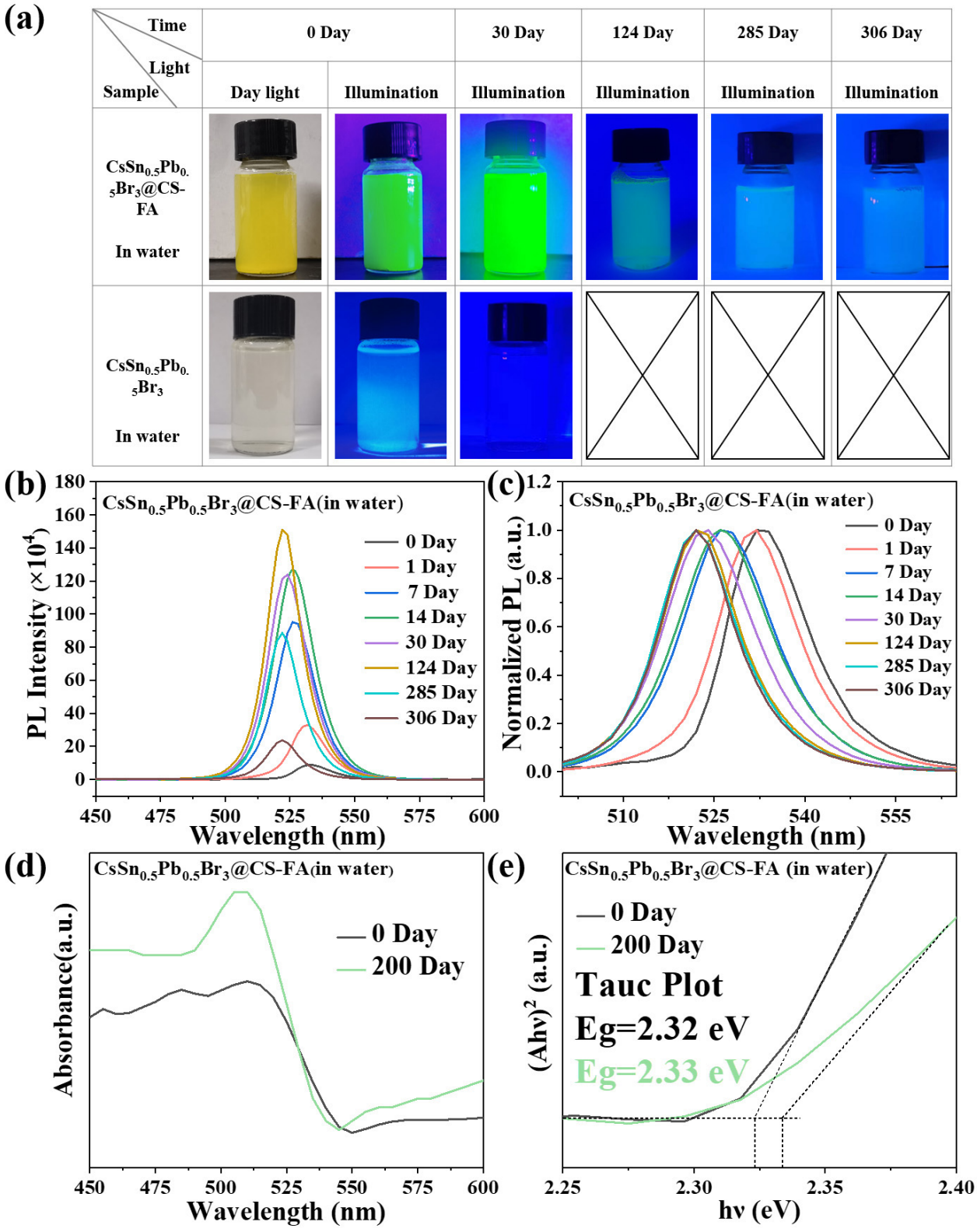

Fig. 4. Optical characterization of $CsSn_{0.5}Pb_{0.5}Br_3$@CS-FA nanoparticles after aqueous storage. (a) Photographs showing the stability of $CsSn_{0.5}Pb_{0.5}Br_3$ NCs and $CsSn_{0.5}Pb_{0.5}Br_3$@CS-FA nanoparticles in aqueous environments. (b,c) PL and normalized PL spectra of $CsSn_{0.5}Pb_{0.5}Br_3$@CS-FA nanoparticles. (d,e) UV-visible spectra and band gap of $CsSn_{0.5}Pb_{0.5}Br_3$@CS-FA nanoparticles.

development and Sn–Pb alloying strategies in halide perovskites has been further investigated in recent reviews [30,31], while the historical discovery of perovskite halides dates back to early work on cesium lead halides [32].

FTIR spectroscopy was used to verify anchoring of chitosan-folic acid (CS-FA) onto $CsSn_{0.5}Pb_{0.5}Br_3$ NCs (Fig. 1b). The amide-bond peak (N-C=O) at 1530 cm^{-1} indicated formation of an amide bond between the carboxyl group of FA and the amino group of CS [33]. The C=C-C=O group of FA was observed at 1637 cm^{-1} [34,35], and the -OH group of CS was detected at 3453 cm^{-1} [34]. A $-CH_3$ peak at 2925 cm^{-1} was attributed to oleic acid and oleylamine used in the synthesis process [36]. These findings confirm successful encapsulation of $CsSn_{0.5}Pb_{0.5}Br_3$ with CS-FA.

TEM analysis showed that $CsSn_{0.5}Pb_{0.5}Br_3$ nanoparticles had a regular and uniform rectangular morphology (Fig. 2a). High-resolution TEM (Fig. 2b) revealed well-resolved lattice fringes with an average interplanar spacing of 0.59 nm, consistent with the (101) plane calculated from XRD patterns. Fast Fourier transform (Fig. 2b, inset) and selected-area electron diffraction (Fig. 2c) further confirmed the crystalline structure of $CsSn_{0.5}Pb_{0.5}Br_3$. Based on the selected-area electron diffraction (SAED) pattern calibrated with the 10 nm^{-1} scale bar, the measured diffraction-ring radius corresponds to a real-space interplanar spacing of approximately 0.59 nm, which is in good agreement with the (101) plane from XRD. After CS-FA coating, $CsSn_{0.5}Pb_{0.5}Br_3$@CS-FA nanoparticles were spherical, with CS-FA uniformly distributed on the $CsSn_{0.5}Pb_{0.5}Br_3$ surface to form a core-shell structure (Fig. 2d). The interplanar spacings of the (121) and (202) planes (Fig. 2e) were 0.44 nm and 0.29 nm, respectively, indicating successful coating of $CsSn_{0.5}Pb_{0.5}Br_3$ NCs with CS-FA. Selected-area electron diffraction (Fig. 2f) validated the crystalline nature of the coated nanoparticles, and the corresponding d-spacings calculated from the SAED pattern are consistent with the high-resolution transmission electron microscopy (HRTEM) observations.

Water Stability of $CsSn_{0.5}Pb_{0.5}Br_3$@CS-FA Nanoparticles

IVIS Lumina III was used to capture fluorescence images of $CsSn_{0.5}Pb_{0.5}Br_3$@CS-FA nanoparticles dispersed in water over 329 days. The nanoparticles maintained detectable fluorescence intensity in aqueous solution throughout this period, indicating long-term fluorescence stability (Fig. 3).

When $CsSn_{0.5}Pb_{0.5}Br_3$ NCs and $CsSn_{0.5}Pb_{0.5}Br_3$@CS-FA nanoparticle powder were dispersed in water, the fluorescence of uncoated $CsSn_{0.5}Pb_{0.5}Br_3$ NCs nearly disappeared within 30 days, whereas $CsSn_{0.5}Pb_{0.5}Br_3$@CS-FA nanoparticles retained fluorescence for 306 days (Fig. 4a). PL spectra further confirmed that fluorescence persisted after long-term storage in water, although the PL peak showed a blue shift from 533 nm to 522 nm from day 0 to day 306 (Fig. 4b,c). UV-visible spectra obtained on day 0 and day 200 showed clear absorption peaks (Fig. 4d), and the calculated energy band gaps were 2.32 eV and 2.33 eV, respectively (Fig. 4e). These data demonstrated excellent water stability and supported further application of $CsSn_{0.5}Pb_{0.5}Br_3$@CS-FA nanoparticles in bioimaging.

In Vitro Targeting and Biocompatibility

Confocal microscopy was used to evaluate the feasibility of $CsSn_{0.5}Pb_{0.5}Br_3$@CS-FA nanoparticles for cellular bioimaging (n = 3) [37]. After 6 h of co-incubation with LLC cells, $CsSn_{0.5}Pb_{0.5}Br_3$@CS-FA nanoparticles showed favorable cellular uptake and relatively uniform intracellular distribution (Fig. 5).

To further assess targeting ability, fluorescence intensity was compared between LLC and C2C12 cells after 6 h of nanoparticle incubation (n = 3). LLC cells showed significantly stronger fluorescence than C2C12 cells ($p < 0.001$, Fig. 6a). Quantitative analysis of fluorescence intensity in LLC cells versus C2C12 cells is shown in Fig. 6a, and comparison between $CsSn_{0.5}Pb_{0.5}Br_3$@CS-FA and non-targeted $CsSn_{0.5}Pb_{0.5}Br_3$@CS nanoparticle treatment in LLC cells is shown in Fig. 6b. Fluorescence intensity in LLC cells treated with $CsSn_{0.5}Pb_{0.5}Br_3$@CS-FA nanoparticles was higher than that in cells treated with $CsSn_{0.5}Pb_{0.5}Br_3$@CS nanoparticles ($p < 0.001$), which is consistent with a possible FA-mediated targeting effect, but this interpretation remains preliminary in the absence of competitive inhibition or receptor-blocking experiments.

Calcein-AM/PI staining was used to evaluate *in vitro* safety (n = 3) [38]. After LLC cells were co-incubated with 0 or 200 μg/mL $CsSn_{0.5}Pb_{0.5}Br_3$@CS-FA nanoparticles for 24 h, no obvious increase in cell death was observed (Fig. 7a). CCK-8 assay was then used to further examine cytotoxicity after treatment with 0–500 μg/mL nanoparticles (n = 6 wells per concentration) [39]. At 200 μg/mL, LLC cell viability remained above 90%, indicating no obvious cytotoxicity at the concentration used for the imaging experiments (Fig. 7b). At higher concentrations (≥300 μg/mL), cell viability gradually decreased to approximately 30% at 500 μg/mL, suggesting a dose-dependent effect. This indicates that, although 200 μg/mL is well tolerated, substantially higher concentrations may require caution in future applications due to the potential risk of cytotoxic effects.

In Vivo Targeting and Biosafety

IVIS Lumina III was used to determine the *in vivo* tumor-targeting capacity of $CsSn_{0.5}Pb_{0.5}Br_3$@CS-FA nanoparticles in tumor-bearing mice (n = 3 mice per group) [40,41]. Before nanoparticle injection, fluorescence signals were not detected in subcutaneous tumors. After tail-vein injection, fluorescence was detected in the tumor region as early as 0.5 h, indicating tumor recognition by FA-modified nanoparticles. Real-time IVIS monitoring showed that flu-

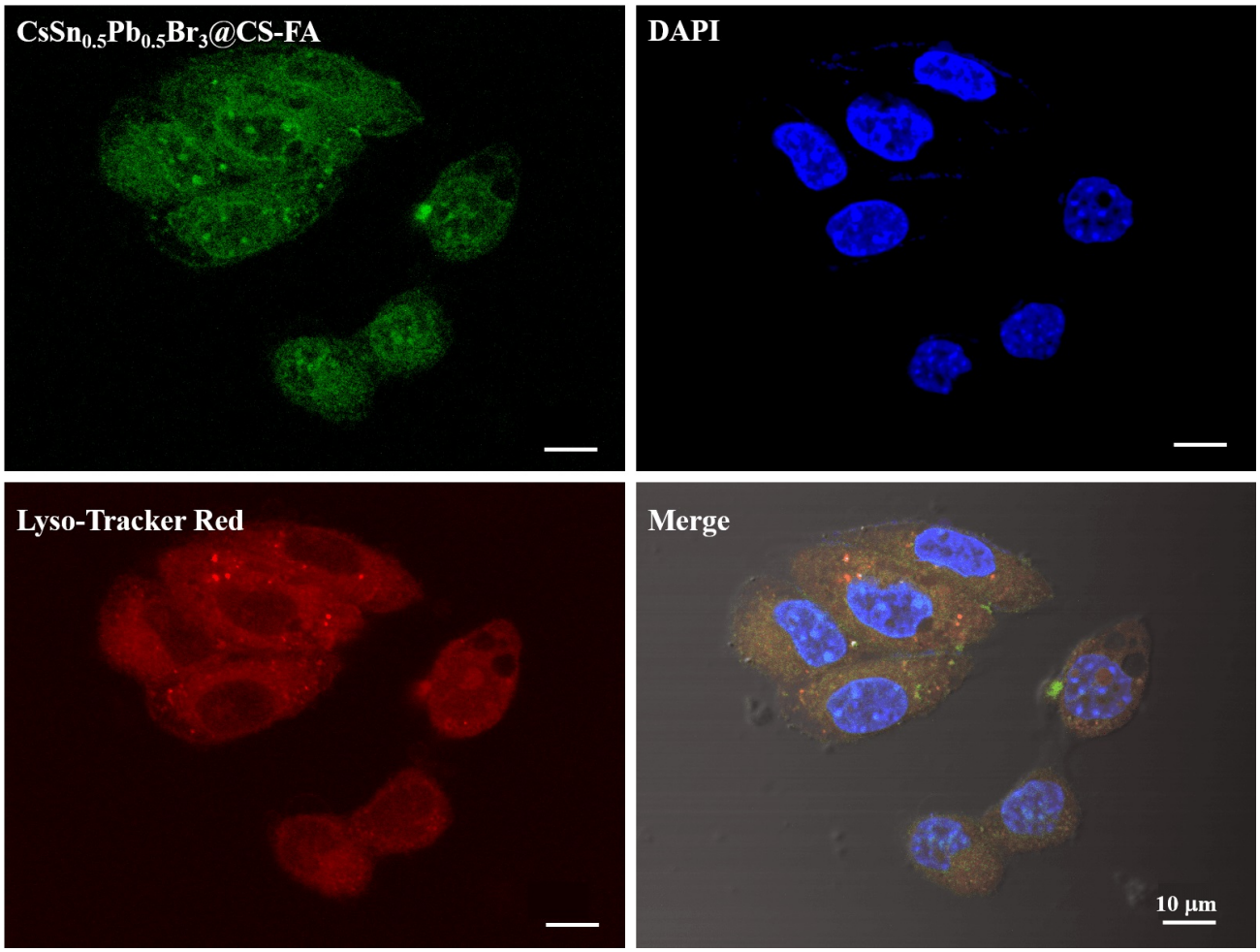

Fig. 5. Confocal fluorescence imaging of LLC cells incubated with $CsSn_{0.5}Pb_{0.5}Br_3$@CS-FA nanoparticles. Representative confocal microscopy images of LLC cells co-incubated with $CsSn_{0.5}Pb_{0.5}Br_3$@CS-FA nanoparticles for 6 h. LLC, Lewis lung carcinoma.

orescence signal intensity gradually increased, reached a maximum at 24 h, and then decreased over time (Fig. 8a,b). No detectable signal was observed after 216 h, suggesting that the nanoparticles may have been progressively cleared or redistributed. The relatively large error bars in Fig. 8b may reflect inter-individual variability in nanoparticle distribution, tumor vascularization, and clearance rates among tumor-bearing mice. To address this, we implemented computer-generated randomization and blinded assessment procedures; however, the small sample size (n = 3 for *in vivo* imaging) remains a potential contributor to the observed variability.

Biosafety was evaluated using histological analysis, hematological testing, liver and renal function testing, and body-weight monitoring. H&E staining of major organs, including the heart, liver, spleen, lung, and kidney, did not reveal obvious tissue injury after $CsSn_{0.5}Pb_{0.5}Br_3$@CS-FA nanoparticle administration (n = 2 mice per group) (Fig. 9) [41,42].

Routine blood parameters showed no statistically significant differences between the $CsSn_{0.5}Pb_{0.5}Br_3$@CS-FA group and the control group (n = 3 per group) (Fig. 10a–e). The data for hemoglobin (HGB, Fig. 10f), liver function indicators (ALT, GGT, and AST, Fig. 10g–i), renal function indicators (Urea and CREA, Fig. 10j,k), and body weight (Fig. 10l) also showed no statistically significant differences between the two groups. These findings suggest favorable short-term *in vivo* biocompatibility of $CsSn_{0.5}Pb_{0.5}Br_3$@CS-FA nanoparticles.

Preliminary Diagnostic Performance in Clinical CSF Samples

A total of 14 patients were included, comprising 7 patients with LC and 7 non-LC controls. All 7 patients in the LC group had positive CSF cytology and were diagnosed as confirmed LC according to the EANO-ESMO criteria. Patients in the non-LC group did not meet the diagnostic criteria for LC. Flow cytometry was used to measure the fluorescence intensity of $CsSn_{0.5}Pb_{0.5}Br_3$@CS-FA nanoparticles in clinical CSF samples (n = 3 technical replicates per sample; flow cytometry collected 10,000 events per sample). The fluorescence intensity was 47.08% ± 13.56% in

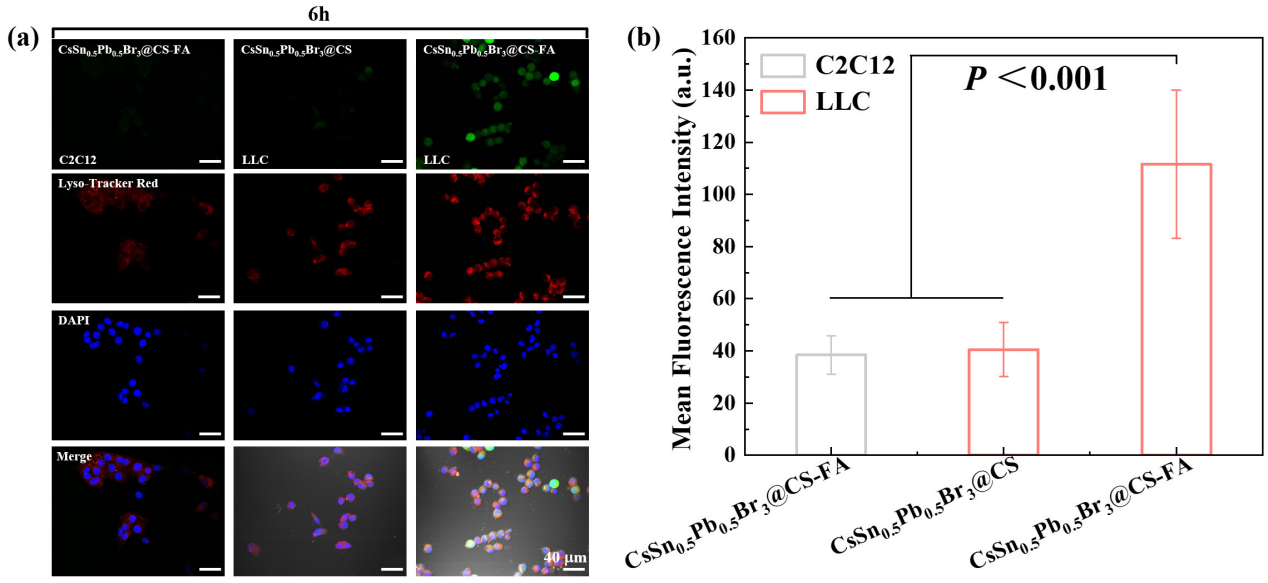

Fig. 6. ***In vitro*** **targeting ability of $CsSn_{0.5}Pb_{0.5}Br_3$@CS-FA nanoparticles**. (a) Confocal microscopy observations and quantification of FA-mediated targeting in C2C12 and LLC cells. (b) Quantification of fluorescence signal intensity comparing CsSn0.5Pb0.5Br3@CS-FA and non-targeted CsSn0.5Pb0.5Br3@CS nanoparticle treatment in LLC cells. Statistical analysis was performed using ImageJ. Data are presented as mean ± SD (n = 3).

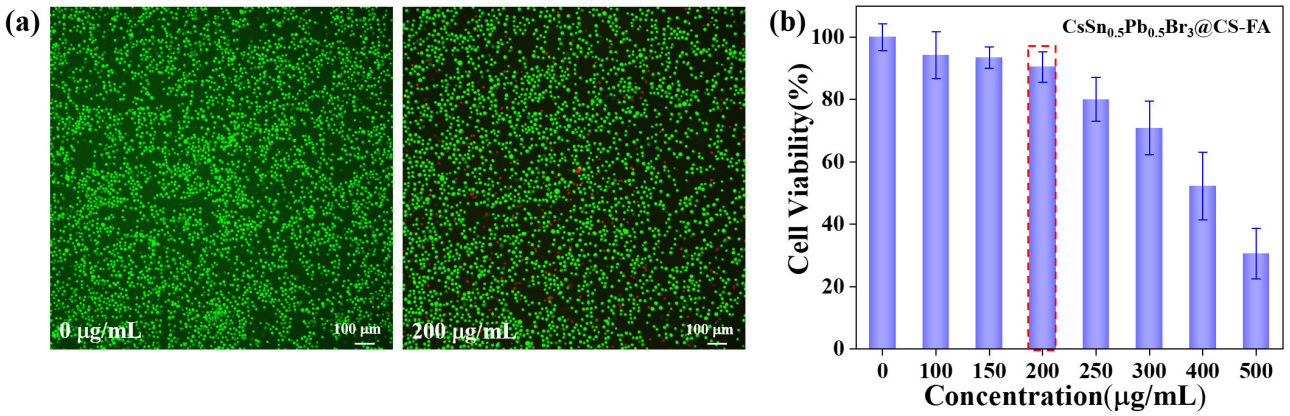

Fig. 7. ***In vitro*** **biocompatibility of $CsSn_{0.5}Pb_{0.5}Br_3$@CS-FA nanoparticles**. (a) Representative Calcein-AM/PI staining images. (b) LLC cell viability after treatment with different concentrations of $CsSn_{0.5}Pb_{0.5}Br_3$@CS-FA nanoparticles. Data are presented as mean ± SD (n = 6 wells per concentration).

the LC group and 2.75% ± 1.12% in the non-LC group, with a statistically significant difference between groups ($p < 0.001$, Fig. 11a,b). Regarding the apparent discrepancy between the representative flow plots in Fig. 11a and the quantified bar graph in Fig. 11b, Fig. 11a displays representative single-sample flow cytometry plots for illustrative purposes, whereas Fig. 11b presents the mean ± SD of fluorescence percentages across all samples in each group (n = 7 per group). The individual variability among clinical samples accounts for the difference between the representative single-plot values and the group averages. This is consistent with the expected heterogeneity in tumor cell content among clinical CSF specimens. These findings suggest that $CsSn_{0.5}Pb_{0.5}Br_3$@CS-FA nanoparticles may serve as a fluorescent tracer for the preliminary detection of LC-associated tumor cells in CSF.

Discussion

Perovskite materials have attracted substantial attention because of their favorable optoelectronic properties and expanding biomedical applications [11,31]. However, conventional perovskite nanomaterials are constrained by poor water stability, potential toxicity, and insufficient tumor targeting. In this study, we synthesized $CsSn_{0.5}Pb_{0.5}Br_3$@CS-FA nanoparticles using a water-triggered strategy [43,44].

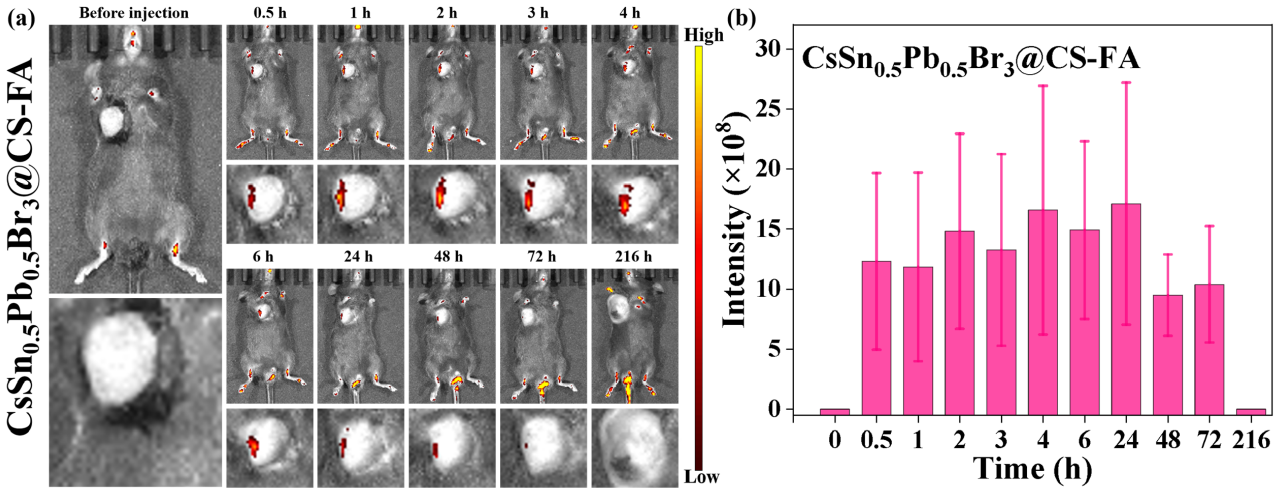

Fig. 8. ***In vivo*** **tumor-targeting ability of $CsSn_{0.5}Pb_{0.5}Br_3$@CS-FA nanoparticles**. (a) IVIS images of $CsSn_{0.5}Pb_{0.5}Br_3$@CS-FA nanoparticles in tumor-bearing mice at 0 and 216 h. (b) Quantification of fluorescence signal intensity from IVIS images. Data are presented as mean ± SD (n = 3 mice per group).

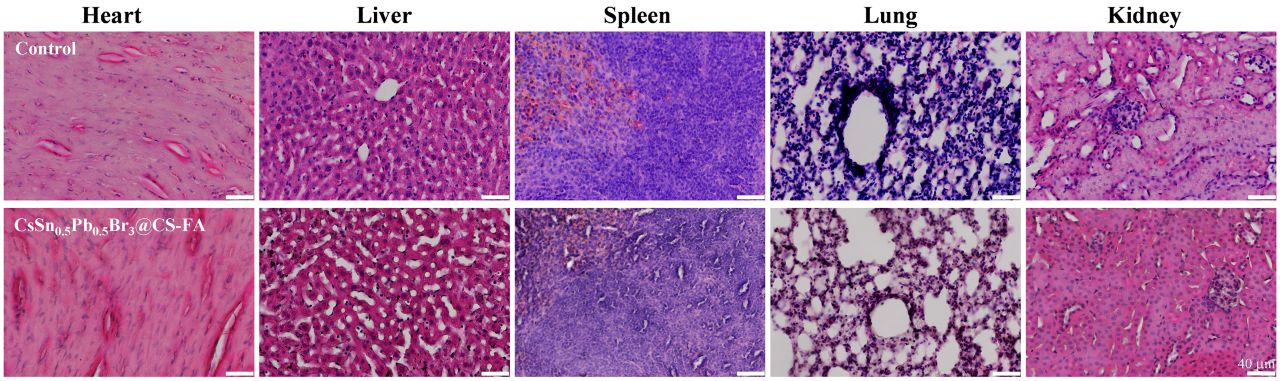

Fig. 9. Histological evaluation of major organs after nanoparticle administration. H&E staining images of major organs from healthy C57BL/6JNifdc mice injected with $CsSn_{0.5}Pb_{0.5}Br_3$@CS-FA nanoparticles. H&E, hematoxylin-eosin.

The design integrated partial Sn substitution to mitigate Pb-associated toxicity, CS coating to improve aqueous stability, and FA modification to enhance tumor targeting. The resulting nanoparticles showed stable fluorescence, favorable cellular uptake, *in vivo* tumor accumulation, and preliminary capacity to distinguish CSF samples from patients with LC and non-LC controls.

The structural characterization results supported successful fabrication of the intended nanomaterial. XRD confirmed that the perovskite-related crystalline structure was maintained after CS-FA coating, while FTIR identified the characteristic amide bond between FA and CS, indicating successful construction of the CS-FA conjugate. TEM further showed that $CsSn_{0.5}Pb_{0.5}Br_3$@CS-FA nanoparticles formed a core-shell-like structure, suggesting uniform coating of $CsSn_{0.5}Pb_{0.5}Br_3$ by CS-FA. These findings are consistent with the functional purpose of the design: CS provided a hydrophilic protective shell, while FA offered a tumor-targeting ligand.

Water stability is critical for bioimaging applications because biological fluids are aqueous environments. Uncoated perovskite NCs are typically unstable in water, which severely limits biomedical use. In the present study, $CsSn_{0.5}Pb_{0.5}Br_3$@CS-FA nanoparticles maintained fluorescence signals in water for several months, whereas uncoated $CsSn_{0.5}Pb_{0.5}Br_3$ NCs lost fluorescence rapidly. PL and UV-visible spectra further indicated preservation of optical characteristics during long-term aqueous storage. This improved stability may be attributed to the CS-containing shell, which limits direct water-induced degradation of the perovskite core.

Both *in vitro* and *in vivo* findings supported the tumor-targeting and biosafety profile of $CsSn_{0.5}Pb_{0.5}Br_3$@CS-FA nanoparticles. LLC cells exhibited stronger fluorescence than C2C12 cells after nanoparticle incubation, and FA-modified nanoparticles produced stronger cellular fluorescence signals than non-targeted nanoparticles. These results are consistent with the targeting role of FA. In tumor-

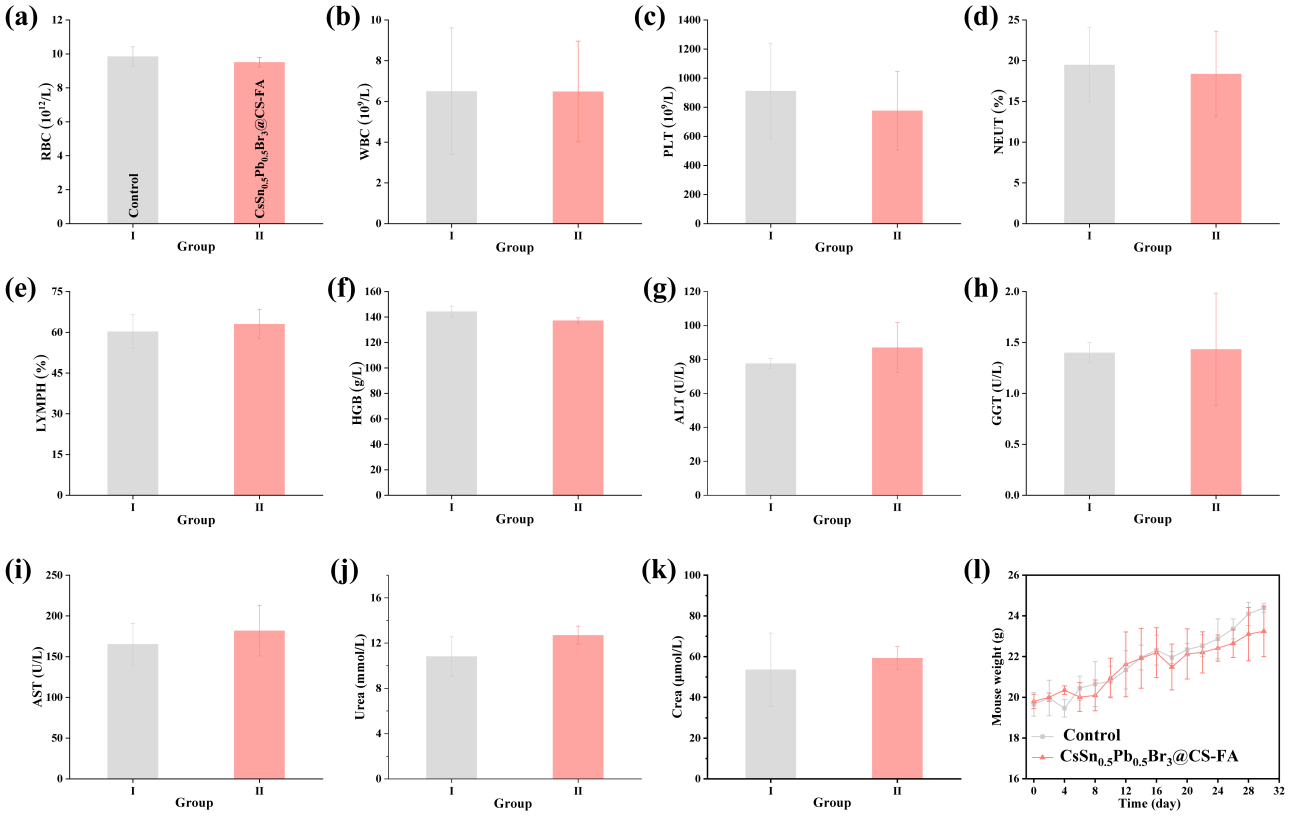

Fig. 10. Hematological, biochemical, and body-weight evaluation after nanoparticle administration. Routine blood parameters including RBC (a), WBC (b), PLT (c), NEUT (d), and LYMPH (e); hemoglobin (HGB) (f); liver function indicators including ALT (g), GGT (h), and AST (i); renal function indicators including Urea (j) and CREA (k); and body weight (l) in healthy mice treated with saline or $CsSn_{0.5}Pb_{0.5}Br_3$@CS-FA nanoparticles. Data are presented as mean ± SD (n = 3 for blood/biochemistry; n = 5 initially per group for body-weight monitoring). RBC, red blood cells; WBC, white blood cells; PLT, platelets; NEUT, neutrophils; LYMPH, lymphocytes; HGB, hemoglobin; ALT, alanine aminotransferase; GGT, gamma-glutamyl transferase; AST, aspartate aminotransferase; Urea, blood urea nitrogen; CREA, creatinine.

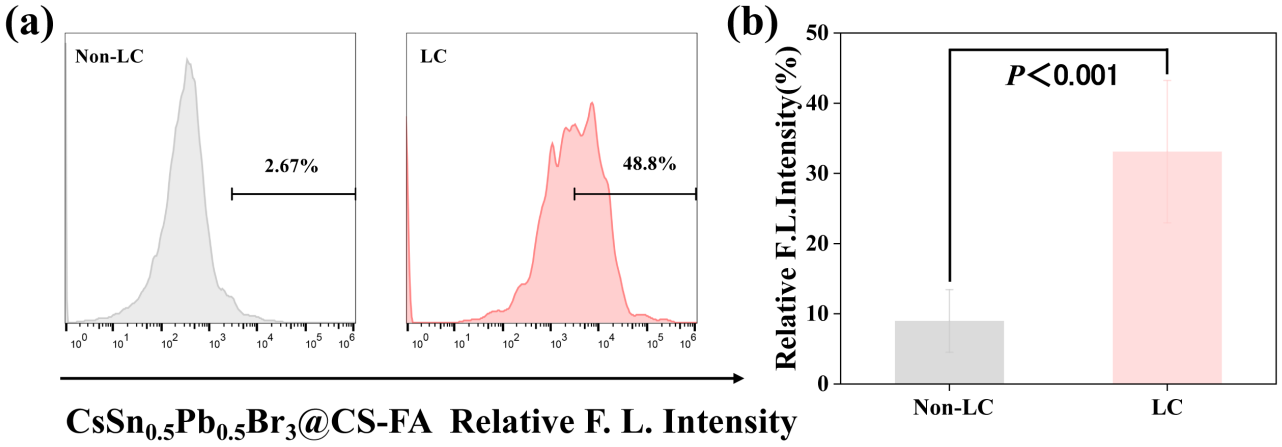

Fig. 11. Fluorescence detection of $CsSn_{0.5}Pb_{0.5}Br_3$@CS-FA nanoparticles in CSF samples from patients with LC. (a) Representative flow-cytometric detection of fluorescence signal intensity in a single CSF sample from a patient with LC and a single non-LC control sample (showing 48.8% and 2.67%, respectively). (b) Quantification of fluorescence signal intensity from flow-cytometric analysis showing group means. Data are presented as mean ± SD (n = 7 per group). CSF, cerebrospinal fluid; LC, Leptomeningeal carcinomatosis; SD, standard deviation.

bearing mice, IVIS imaging showed tumor-localized fluorescence after intravenous injection, and the signal gradually decreased by 216 h. Short-term safety evaluation did not reveal obvious cytotoxicity, organ damage, hematological toxicity, liver or renal dysfunction, or body-weight loss. These data suggest that $CsSn_{0.5}Pb_{0.5}Br_3$@CS-FA nanoparticles exhibit acceptable preliminary biocompatibility for further preclinical evaluation.

The clinical CSF experiment provides preliminary evidence for diagnostic relevance. Fluorescence intensity was markedly higher in CSF samples from patients with LC than in non-LC controls. Because CSF cytology has limited sensitivity and repeated lumbar puncture is often required in clinical practice, a fluorescence-based tumor-cell labeling strategy may provide complementary information. However, the present findings should be interpreted as exploratory rather than confirmatory.

This study has several limitations. First, the clinical sample size was small, with only 7 patients in each group; therefore, the findings mainly support feasibility and cannot fully establish diagnostic performance. Second, no independent validation cohort was included, and diagnostic indices such as the receiver operating characteristic curve, area under the curve, sensitivity, specificity, positive predictive value, and negative predictive value were not calculated. Third, the *in vivo* experiments used a subcutaneous tumor model, which can demonstrate tumor targeting and systemic biosafety but does not fully reproduce CSF dissemination, meningeal involvement, the blood-brain barrier, or the central nervous system microenvironment of LC. Fourth, the observation period for *in vivo* safety was limited, and long-term metabolism, tissue accumulation, clearance, and neurotoxicity remain uncertain. Future studies should include larger multicenter cohorts, independent validation, orthotopic or leptomeningeal metastasis models, and extended toxicological assessments.

Conclusion

This study successfully developed $CsSn_{0.5}Pb_{0.5}Br_3$@CS-FA nanoparticles with favorable water stability, fluorescence performance, tumor-targeting ability, and preliminary biocompatibility. *In vitro* and *in vivo* experiments suggest that these nanoparticles can be used for tumor-cell fluorescence imaging, and clinical CSF testing shows stronger fluorescence signals in patients with LC than in non-LC controls. These results indicate that $CsSn_{0.5}Pb_{0.5}Br_3$@CS-FA nanoparticles may have potential as an auxiliary fluorescent tracer for LC diagnosis. Further validation in larger clinical cohorts and more clinically relevant animal models is required before translation into clinical practice.

Availability of Data and Materials

The datasets used or analyzed during the current study are available from the corresponding author upon reasonable request.

Author Contributions

JL, HB and YZ designed the research study. RRY, RHL and YNJ performed the research. SYC, JL and HB analyzed the data. JL, YNJ drafted the article. All authors contributed to important editorial changes in the manuscript. All authors read and approved the final manuscript. All authors have participated sufficiently in the work and agreed to be accountable for all aspects of the work.

Ethics Approval and Consent to Participate

The animal experiments were approved by the Ethics Committee of the Second Hospital of Hebei Medical University (No. 2023-AE085). The clinical study was approved by the Ethics Committee of the Second Hospital of Hebei Medical University (No. 2023-R360). Written informed consent was obtained from all patients or their legal representatives. The clinical study was conducted in accordance with the Declaration of Helsinki. Animal experiments were conducted in accordance with the ARRIVE 2.0 Guidelines.

Acknowledgment

Not applicable.

Funding

This work was supported by the Central Government Guide Local Science and Technology Development Fund Project (Science and Technology Innovation Base Project) (No. 236Z7753G).

Conflict of Interest

The authors declare no conflict of interest.

References

[1] Siegel RL, Miller KD, Jemal A. Cancer statistics, 2020. CA: A Cancer Journal for Clinicians. 2020; 70: 7–30. https://doi.org/10.3322/caac.21590

[2] McPhail S, Johnson S, Greenberg D, Peake M, Rous B. Stage at diagnosis and early mortality from cancer in England. British Journal of Cancer. 2015; 112 Suppl 1: S108–S115. https://doi.org/10.1038/bjc.2015.49

[3] Mollica L, Leli C, Puglisi S, Sardi S, Sottotetti F. Leptomeningeal carcinomatosis and breast cancer: a systematic review of current evidence on diagnosis, treatment and prognosis. Drugs in Context. 2021; 10: 2021–2021–6–6. https://doi.org/10.7573/dic.2021-6-6

[4] Weissleder R, Nahrendorf M. Advancing biomedical imaging. Proceedings of the National Academy of Sciences of the United States of America. 2015; 112: 14424–14428. https://doi.org/10.1073/pnas.1508524112

[5] Chen G, Roy I, Yang C, Prasad PN. Nanochemistry and Nanomedicine for Nanoparticle-based Diagnostics and Therapy. Chemical Reviews. 2016; 116: 2826–2885. https://doi.org/10.1021/acs.chemrev.5b00148

[6] Heinzmann K, Carter LM, Lewis JS, Aboagye EO. Multiplexed imaging for diagnosis and therapy. Nature Biomedical Engineering. 2017; 1: 697–713. https://doi.org/10.1038/s41551-017-0131-8

[7] Hong G, Diao S, Chang J, Antaris AL, Chen C, Zhang B, et al. Through-skull fluorescence imaging of the brain in a new near-infrared window. Nature Photonics. 2014; 8: 723–730. https://doi.org/10.1038/nphoton.2014.166

[8] Dang X, Bardhan NM, Qi J, Gu L, Eze NA, Lin CW, et al. Deep-tissue optical imaging of near cellular-sized features. Scientific Reports. 2019; 9: 3873. https://doi.org/10.1038/s41598-019-39502-w

[9] Koscher BA, Swabeck JK, Bronstein ND, Alivisatos AP. Essentially Trap-Free $CsPbBr_3$ Colloidal Nanocrystals by Postsynthetic Thiocyanate Surface Treatment. Journal of the American Chemical Society. 2017; 139: 6566–6569. https://doi.org/10.1021/jacs.7b02817

[10] Dai SW, Hsu BW, Chen CY, Lee CA, Liu HY, Wang HF, et al. Perovskite Quantum Dots with Near Unity Solution and Neat-Film Photoluminescent Quantum Yield by Novel Spray Synthesis. Advanced Materials (Deerfield Beach, Fla.). 2018; 30: 1705532. https://doi.org/10.1002/adma.201705532

[11] Wang Z, Fu R, Li F, Xie H, He P, Sha Q, et al. One-Step Polymeric Melt Encapsulation Method to Prepare CsPbBr3 Perovskite Quantum Dots/Polymethyl Methacrylate Composite with High Performance. Advanced Functional Materials. 2021; 31: 2010009.

[12] He C-L, Meng Z-Q, Ren S-X, Li J, Wang Y, Wu H, et al. Water-ultrastable perovskite CsPbBr3 nanocrystals for fluorescence-enhanced cellular imaging. Rare Metals. 2023; 42: 1624–1634.

[13] Aktas E, Rajamanickam N, Pascual J, Hu S, Aldamasy MH, Di Girolamo D, et al. Challenges and strategies toward long-term stability of lead-free tin-based perovskite solar cells. Communications Materials. 2022; 3: 104.

[14] Ramezani Farani M, Azarian M, Heydari Sheikh Hossein H, Abdolvahabi Z, Mohammadi Abgarmi Z, Moradi A, et al. Folic Acid-Adorned Curcumin-Loaded Iron Oxide Nanoparticles for Cervical Cancer. ACS Applied Bio Materials. 2022; 5: 1305–1318. https://doi.org/10.1021/acsabm.1c01311

[15] Wang C, Wang Q, Wang H, Li Z, Chen J, Zhang Z, et al. Hydroxyethyl starch-folic acid conjugates stabilized theranostic nanoparticles for cancer therapy. Journal of Controlled Release : Official Journal of the Controlled Release Society. 2023; 353: 391–410. https://doi.org/10.1016/j.jconrel.2022.11.059

[16] Le Rhun E, Weller M, van den Bent M, Brandsma D, Furtner J, Rudà R, et al. Leptomeningeal metastasis from solid tumours: EANO-ESMO Clinical Practice Guideline for diagnosis, treatment and follow-up. ESMO Open. 2023; 8: 101624. https://doi.org/10.1016/j.esmoop.2023.101624

[17] Pramanik A, Patibandla S, Gao Y, Gates K, Ray PC. Water Triggered Synthesis of Highly Stable and Biocompatible 1D Nanowire, 2D Nanoplatelet, and 3D Nanocube $CsPbBr_3$ Perovskites for Multicolor Two-Photon Cell Imaging. JACS Au. 2021; 1: 53–65. https://doi.org/10.1021/jacsau.0c00038

[18] Liu F, Ding C, Zhang Y, Ripolles TS, Kamisaka T, Toyoda T, et al. Colloidal Synthesis of Air-Stable Alloyed $CsSn_{1-x}Pb_xI_3$ Perovskite Nanocrystals for Use in Solar Cells. Journal of the American Chemical Society. 2017; 139: 16708–16719. https://doi.org/10.1021/jacs.7b08628

[19] Schwartz HA, Laurenzen H, Marzouk A, Runkel M, Brinkmann KO, Rogalla D, et al. Band-Gap Tuning in All-Inorganic $CsPb_xSn_{1-x}Br_3$ Perovskites. ACS Applied Materials & Interfaces. 2021; 13: 4203–4210. https://doi.org/10.1021/acsami.0c20285

[20] Karmakar A, Bhattacharya A, Bernard GM, Mar A, Michaelis VK. Revealing the Local Sn and Pb Arrangements in CsSnxPb1-xBr3 Perovskites with Solid-State NMR Spectroscopy. ACS Materials Letters. 2021; 3: 261–267.

[21] Xian Y, Zhang Y, Rahman NU, Yin H, Long Y, Liu P, et al. An Emerging All-Inorganic CsSnxPb1-xBr3 ($0 \leq x \leq 1$) Perovskite Single Crystal: Insight on Structural Phase Transition and Electronic Properties. Journal of Physical Chemistry C. 2020; 124: 13434–13446.

[22] Zhang H, Lee JW, Nasti G, Handy R, Abate A, Grätzel M, et al. Lead immobilization for environmentally sustainable perovskite solar cells. Nature. 2023; 617: 687–695. https://doi.org/10.1038/s41586-023-05938-4

[23] Chowdhury TH, Reo Y, Yusoff ARBM, Noh YY. Sn-Based Perovskite Halides for Electronic Devices. Advanced Science (Weinheim, Baden-Wurttemberg, Germany). 2022; 9: e2203749. https://doi.org/10.1002/advs.202203749

[24] Sun Q, Zhang Z, Zhang T, Feng Y, Gu A, Yu H, et al. Integrated 4-Terminal All-Inorganic Perovskite Tandem Solar Cell with Open-Circuit Voltage Exceeding 2.1 V for Water Splitting. ACS Energy Letters. 2022; 7: 4215–4223.

[25] Xia Y, Chen Y, Luo T, Liang H, Gao Y, Xu X, et al. Unexpected bowing band evolution in an all-inorganic $CsSn_{1-x}$ Pb_x Br_3 perovskite. RSC Advances. 2020; 10: 26407–26413. https://doi.org/10.1039/d0ra03709e

[26] Calcabrini M, Genç A, Liu Y, Kleinhanns T, Lee S, Dirin DN, et al. Exploiting the Lability of Metal Halide Perovskites for Doping Semiconductor Nanocomposites. ACS Energy Letters. 2021; 6: 581–587. https://doi.org/10.1021/acsenergylett.0c02448

[27] Yang Z, Zhang S, Sheng T, Lv X, Wei X, Qin S, et al. Phase engineering of inorganic halide Cs-Pb-Br perovskites for advanced energy conversion. Journal of Materials Chemistry A. 2023; 11: 22020–22040.

[28] He Q, Mei E, Liang X, Xiang W. Ultrastable PVB films-protected CsPbBr3/Cs4PbBr6 perovskites with high color purity for nearing Rec. 2020 standard. Chemical Engineering Journal. 2021; 419: 129529.

[29] Song L, Huang L, Liu Y, Hu Y, Guo X, Chang Y, et al. Efficient and Stable Blue Perovskite Light-Emitting Devices Based on Inorganic Cs_4PbBr_6 Spaced Low-Dimensional $CsPbBr_3$ through Synergistic Control of Amino Alcohols and Polymer Additives. ACS Applied Materials & Interfaces. 2021; 13: 33199–33208. https://doi.org/10.1021/acsami.1c02555

[30] Macdonald TJ, Lanzetta L, Liang X, Ding D, Haque SA. Engineering Stable Lead-Free Tin Halide Perovskite Solar Cells: Lessons from Materials Chemistry. Advanced Materials (Deerfield Beach, Fla.). 2023; 35: e2206684. https://doi.org/10.1002/adma.202206684

[31] Liang S, Zhang M, Biesold GM, Choi W, He Y, Li Z, et al. Recent Advances in Synthesis, Properties, and Applications of Metal Halide Perovskite Nanocrystals/Polymer Nanocomposites. Advanced Materials (Deerfield Beach, Fla.). 2021; 33: e2005888. https://doi.org/10.1002/adma.202005888

[32] Wells HL. Über die cäsium-und kalium-bleihalogenide. Zeitschrift für anorganische Chemie. 1893; 3: 195–210. (In German)

[33] St. Thomas. Spectroscopic Tools. Available at: http://www.science-and-fun.de/tools (Accessed: 30 Jun 2026).

[34] Al-Nemrawi N, Hameedat F, Al-Husein B, Nimrawi S. Photolytic Controlled Release Formulation of Methotrexate Loaded

in Chitosan/TiO_2 Nanoparticles for Breast Cancer. Pharmaceuticals (Basel, Switzerland). 2022; 15: 149. https://doi.org/10.3390/ph15020149

[35] Al-Nemrawi NK, Altawabeyeh RM, Darweesh RS. Preparation and Characterization of Docetaxel-PLGA Nanoparticles Coated with Folic Acid-chitosan Conjugate for Cancer Treatment. Journal of Pharmaceutical Sciences. 2022; 111: 485–494. https://doi.org/10.1016/j.xphs.2021.10.034

[36] Li M, Zhang X, Yang P. Controlling the growth of a SiO_2 coating on hydrophobic $CsPbBr_3$ nanocrystals towards aqueous transfer and high luminescence. Nanoscale. 2021; 13: 3860–3867. https://doi.org/10.1039/d0nr08325a

[37] Pandey S, Choudhary P, Gajbhiye V, Jadhav S, Bodas D. In vivo imaging of prostate tumor-targeted folic acid conjugated quantum dots. Cancer Nanotechnology. 2023; 14: 30.

[38] Du J, Zhou M, Chen Q, Tao Y, Ren J, Zhang Y, et al. Disrupting Intracellular Iron Homeostasis by Engineered Metal-Organic Framework for Nanocatalytic Tumor Therapy in Synergy with Autophagy Amplification-Promoted Ferroptosis. Advanced Functional Materials. 2023; 33: 2215244.

[39] Zhou G, Li M. Near-Infrared-II Plasmonic Trienzyme-Integrated Metal-Organic Frameworks with High-Efficiency Enzyme Cascades for Synergistic Trimodal Oncotherapy. Advanced Materials (Deerfield Beach, Fla.). 2022; 34: e2200871. https://doi.org/10.1002/adma.202200871

[40] Lu G, Wang X, Li F, Wang S, Zhao J, Wang J, et al. Engineered biomimetic nanoparticles achieve targeted delivery and efficient metabolism-based synergistic therapy against glioblastoma. Nature Communications. 2022; 13: 4214. https://doi.org/10.1038/s41467-022-31799-y

[41] Feng W, Lv Y, Chen Z, Wang F, Wang Y, Pei Y, et al. A carrier-free multifunctional nano photosensitizer based on self-assembly of lactose-conjugated BODIPY for enhanced antitumor efficacy of dual phototherapy. Chemical Engineering Journal. 2021; 417: 129178.

[42] Niu H, Chen J, Jin J, Qi X, Bai K, Shu C, et al. Engineering metalloporphyrin-integrated nanosystems for targeted sono-/chemo-dynamic therapy of leptomeningeal carcinomatosis through intrathecal administration. Chemical Engineering Journal. 2022; 437: 135373.

[43] Dong H, Kareem S, Gong X, Ruan J, Gao P, Zhou X, et al. Water-Triggered Transformation of Ligand-Free Lead Halide Perovskite Nanocrystal-Embedded Pb(OH)Br with Ultrahigh Stability. ACS Applied Materials & Interfaces. 2021; 13: 23960–23969. https://doi.org/10.1021/acsami.1c06627

[44] Das A, Debnath T. Water-Triggered Chemical Transformation of Perovskite Nanocrystals. Chemistry (Weinheim an Der Bergstrasse, Germany). 2023; 29: e202202475. https://doi.org/10.1002/chem.202202475